

CO MULTI-LINE OBSERVATIONS OF HH 80-81: A TWO-COMPONENT MOLECULAR OUTFLOW ASSOCIATED WITH THE LARGEST PROTOSTELLAR JET IN OUR GALAXY

KEPING QIU,^{1,2} FRIEDRICH WYROWSKI,³ KARL MENTEN,³ QIZHOU ZHANG,⁴ AND ROLF GÜSTEN³

¹*School of Astronomy and Space Science, Nanjing University, 163 Xianlin Avenue, Nanjing 210023, China*

²*Key Laboratory of Modern Astronomy and Astrophysics (Nanjing University), Ministry of Education, Nanjing 210023, China*

³*Max-Planck-Institut für Radioastronomie, Auf dem Hügel 69, 53121 Bonn, Germany*

⁴*Harvard-Smithsonian Center for Astrophysics, 60 Garden Street, Cambridge, MA 02138, U.S.A.*

Submitted to ApJ

ABSTRACT

Stretching a length reaching 10 pc projected in the plane of sky, the radio jet associated with Herbig-Haro objects 80 and 81 (HH 80-81) is known as the largest and best collimated protostellar jet in our Galaxy. The nature of the molecular outflow associated with this extraordinary jet remains an unsolved question which is of great interests to our understanding of the relationship between jets and outflows in high-mass star formation. Here we present Atacama Pathfinder EXperiment CO (6–5) and (7–6), James Clerk Maxwell Telescope CO (3–2), Caltech Submillimeter Observatory CO (2–1), and Submillimeter Array CO and ¹³CO (2–1) mapping observations of the outflow. We report on the detection of a two-component outflow consisting of a collimated component along the jet path and a wide-angle component with an opening angle of about 30°. The gas velocity structure suggests that each of the two components traces part of a primary wind. From LVG calculations of the CO lines, the outflowing gas has a temperature around 88 K, indicating that the gas is being heated by shocks. Based on the CO (6–5) data, the outflow mass is estimated to be a few M_{\odot} , which is dominated by the wide-angle component. A comparison between the HH 80–81 outflow and other well shaped massive outflows suggests that the opening angle of massive outflows continues to increase over time. Therefore, the mass loss process in the formation of early-B stars seems to be similar to that in low-mass star formation, except that a jet component would disappear as the central source evolves to an ultracompact HII region.

Keywords: ISM: individual objects (HH 80-81) — ISM: individual objects (IRAS 18162-2048) — ISM: individual objects (GGD 27) — ISM: jets and outflows — stars: formation — stars: massive

1. INTRODUCTION

Jets and outflows are found to be ubiquitous in the formation of stars of all the masses (see Frank et al. 2014; Bally 2016, for recent reviews). Thanks to their variety of manifestations, e.g., Herbig-Haro (HH) objects, molecular hydrogen objects (MHOs), radio jets, and molecular outflows, they are observable from X-ray to radio wavelengths. Molecular outflows are often observed in rotational transitions of CO and some other molecules (e.g., SiO). They are of particular interests to our understanding of the earliest stages of star formation, when the central protostars are deeply embedded in gas and dust cores which are invisible at optical to near-infrared wavelengths. These outflows are often the first clear sign of the formation of a new star (e.g., Phan-Bao et al. 2008; Tobin et al. 2016; Tan et al. 2016; Feng et al. 2016), and provide insights into the mass accretion process as well as the multiplicity of the central protostars (e.g., Beuther et al. 2002b; Plunkett et al. 2015; Hsieh et al. 2016).

Outflows in low-mass young stellar objects (YSOs) are far better studied, both observationally and theoretically, compared to their counterparts in the high-mass regime. They have long been thought to be ambient material accelerated by an underlying jet or wind moving at velocities of order 100 km s^{-1} (see, e.g., Arce et al. 2007, and references therein), but some extremely high velocity structures may originate from the close vicinity of a central protostar (e.g., Tafalla et al. 2010, 2015), and moreover, there is evidence from new observations that molecular outflows could be directly ejected from an accretion disk (Bjerkeli et al. 2016; Alves et al. 2017; Lee et al. 2017; Tabone et al. 2017; Güdel et al. 2018). It has been noted that interaction between a single collimated jet or a wide-angle wind and the ambient cloud could not explain the full range of observed features of molecular outflows (Cabrit et al. 1997; Lee et al. 2000, 2001, 2002; Arce & Goodman 2002). In particular, high angular resolution observations often show that low-mass protostellar outflows contain a collimated, jet-like component at higher velocities, and a wide-angle, shell-like component at lower velocities (Bachiller et al. 1995; Gueth & Guilloteau 1999; Palau et al. 2006; Santiago-García et al. 2009; Hirano et al. 2010; Lee et al. 2018). Such two-component outflows could be tracing a laterally stratified primary wind, or an axial jet surrounded by a wide-angle wind, breaking out of a dense infalling envelope (Arce & Sargent 2006; Shang et al. 2006). The primary jet or wind is launched through the coupling of magnetic fields and dense gas rotation around the central protostar, but the detailed mechanism is not well understood (see Li et al. 2014, and references therein). Recent Atacama Large Millimeter/submillimeter Array (ALMA) observations suggest that the collimated jet has a launching radius at sub-AU scales on the disk (Lee et al. 2017), whereas the wide-angle wind is ejected from a region up to a radial distance of a few tens of AU on the disk (Bjerkeli et al. 2016; Tabone et al. 2017).

Outflows in high-mass YSOs have sizes and velocity structures similar to those in low-mass outflows, but have orders of magnitude greater masses and energetics (Zhang et al. 2001, 2005; Beuther et al. 2002a; Bally 2016). Based on the statistics of a large sample of CO outflows observed with single-dish telescopes, Wu et al. (2004) find that outflows in luminous sources ($> 10^3 L_{\odot}$) are systemically less collimated than flows in lower luminosity sources. On the other hand, high angular resolution observations made with millimeter or submillimeter interferometers have detected both highly collimated outflows and wide-angle outflows in high-mass YSOs (e.g., Shepherd et al. 1998; Cesaroni et al. 1999; Qiu et al. 2009; Qiu & Zhang 2009; Zhang et al. 2015). There is even an explosive, rather than bipolar, outflow in the well-known Orion BN/KL region (Zapata et al. 2009; Bally et al. 2017). Theoretically, it appears to be a consensus in numerical simulations that outflows would be generated during the collapse of a massive cloud core if magnetic fields are included (Banerjee & Pudritz 2007; Peters et al. 2011; Hennebelle et al. 2011; Commerçon et al. 2011), but the outflow launching zone is not resolved and the simulations were not run long enough to allow a comparison to observations. More recently, a few numerical works focusing on the developing of outflows in high-mass star-forming cores suggest that the disk wind model is applicable to the high-mass regime (Seifried et al. 2012; Kuiper et al. 2015; Matsushita et al. 2018). Since high-mass YSOs are typically far away from the Sun and tend to reside in crowded clusters, there are few observations capable of constraining the launching of their jets and outflows (Carrasco-González et al. 2015; Hirota et al. 2017). Many basic properties of outflows in high-mass YSOs, such as the collimation, excitation conditions, evolution, and driving mechanism, are poorly known. The question that whether outflows in high-mass YSOs are scaled up versions of those in low-mass YSOs remains open.

The radio jet associated with HH objects 80 and 81 is driven from a high-mass YSO with a bolometric luminosity of $2 \times 10^4 L_{\odot}$ at an adopted distance of 1.7 kpc (Rodríguez et al. 1980; Reipurth & Graham 1988; Martí et al. 1993). The jet measured 5.3 pc in projection from HH 80 to a radio source to the north (HH 80 North, Martí et al. 1993), and was updated to 7.5 pc with the detection of an outer bow shock beyond HH 80 (Heathcote et al. 1998) and even

larger to 10.3 pc by including a newly detected radio source along the jet path beyond HH 80 North (Masqué et al. 2012). This makes the HH 80–81 jet far larger than any other YSO jet or HH object known so far. The jet material moves extremely fast with tangential velocities of $\sim 600\text{--}1400\text{ km s}^{-1}$ for the inner knots (Martí et al. 1993, 1995) and of $\sim 200\text{--}400\text{ km s}^{-1}$ for the outer knots (Heathcote et al. 1998; Masqué et al. 2015). If a proposed inclination angle of 56° (from the plane of the sky) is taken into account, the jet length and velocity would be further increased by a factor of 1.8 (Heathcote et al. 1998). It is also one of the few YSO jets showing non-thermal emissions and is the first detected in linearly polarized synchrotron emission attributed to relativistic electrons (Carrasco-González et al. 2010; Rodríguez-Kamenetzky et al. 2017; Vig et al. 2018). The central source of the jet is found to be surrounded by a disk-like structure with a radius of a few 100 AU (Fernández-López et al. 2011b; Girart et al. 2018). The *Spitzer* 8 μm image reveals the wall of a biconical cavity surrounding the radio jet (Qiu et al. 2008). All this makes the HH 80–81 radio jet an ideal target for testing whether protostellar jets and outflows in low-mass and high-mass YSOs share a common driving mechanism. However, the nature of the associated outflow is far less clear. Previous single-dish CO low- J observations detected a parsec-sized outflow in the region, but the maps were of low resolutions (16–45 $''$) and apparently affected by contaminations from ambient gas, and thus could not resolve the morphology and kinematics of the outflow (Yamashita et al. 1989; Ridge & Moore 2001; Benedettini et al. 2004; Wu et al. 2005). Existing interferometer CO (2–1) observations toward the central source of HH 80–81 failed to identify outflow structures associated with the radio jet (Qiu & Zhang 2009; Fernández-López et al. 2013). Here we present CO multi-line observations covering the central parsec area of the radio jet, aimed at identifying and characterizing the molecular outflow associated with this extraordinary jet. We describe our observations in Section 2, and show the results in Section 3. Discussions on the properties of the HH 80–81 outflow, and its implications on a possible evolutionary picture for massive outflows, are presented in Section 4. Finally, a brief summary of this work is given in Section 5.

2. OBSERVATIONS AND DATA REDUCTION

2.1. APEX Observations

We performed CO (6–5) and (7–6) observations on 2010 July 3 with the Atacama Pathfinder EXperiment¹ (APEX) and its Carbon Heterodyne Array of the MPIfR (CHAMP⁺, Kasemann et al. 2006). CHAMP⁺ is a dual-color heterodyne array consisting of 2×7 pixels for spectroscopy in the 450 and 350 μm atmospheric windows. Each of the 14 CHAMP⁺ pixels outputs signals into two 1.5 GHz wide Fast Fourier Transform (FFT) spectrometers configurable for a total bandwidth of 2.4 to 2.8 GHz (corresponding to overlaps of 600 to 200 MHz). We tuned the receiver array to simultaneously observe CO (6–5) at 691 GHz and CO (7–6) at 806 GHz, and configured the spectrometers, each divided into 2048 channels, to have a bandwidth of 2.4 GHz. The APEX beams at these two frequencies are about 9 $.''0$ and 7 $.''7$. We obtained $2' \times 1'5$ maps centered at (R.A., Decl.)_{J2000}=(18^h19^m12^s.1, $-20^\circ 47' 31''$) with the on-the-fly (OTF) mode. The OTF maps were sampled with 40×30 grid cells and a cell size of 3 $.''$, and the long axis was tilted by 19° east of north to follow the orientation of the radio jet. The data were processed with the GILDAS/CLASS package for baseline fitting and subtraction, velocity smoothed into 1 km s^{-1} channels, and re-gridded into cell sizes of 4 $.''5$ and 3 $.''85$ (half of the beams) for CO (6–5) and (7–6), respectively. The final data have an intensity scale in T_{A}^* and the root mean square (RMS) sensitivities are 0.1 K for CO (6–5) and 0.3 K for CO (7–6). For quantitative analyses such as Large Velocity Gradient (LVG) calculations, we convert the intensity scale from T_{A}^* to the main-beam antenna temperature (T_{mb}) with a beam efficiency of 0.41, which was measured toward planets (Jupiter, Mars, and Uranus) in late July 2010.

2.2. CSO Observations

The CO (2–1) observations were undertaken on 2014 July 7 with the Caltech Submillimeter Observatory² (CSO) and its 230 GHz receiver. The output signal was processed by a FFT spectrometer which was configured to have a total bandwidth of 1 GHz divided into 8192 channels. The CSO beam at the frequency of CO (2–1) is about 32 $.''$. We made OTF observations to obtain a map with 11×6 grid cells and a grid cell size of 16 $.''$. The data were processed with the GILDAS/CLASS package for baseline fitting and subtraction, and velocity smoothed into 1 km s^{-1} channels. The calibrated data in T_{A}^* have an RMS sensitivity of 0.2 K. The intensity scale in T_{mb} could be derived with a beam efficiency of 0.70, following <http://www.submm.caltech.edu/cso/receivers/beams.html>.

¹ This publication is based on data acquired with the Atacama Pathfinder Experiment (APEX). APEX is a collaboration between the Max-Planck-Institut für Radioastronomie, the European Southern Observatory, and the Onsala Space Observatory.

² This material is based upon work at the Caltech Submillimeter Observatory, which is operated by the California Institute of Technology.

Table 1. Key parameters of the observed CO lines

Transition	Frequency (GHz)	E_{up}/k (K)	Telescope	Angular Resolution (arcsec)	Velocity Resoluion (km s^{-1})	RMS Sensitivity ^a (K)
$J = 2-1$	230.538	16.6	CSO	32''	1.0	0.2
$J = 2-1$	230.538	16.6	SMA	4.''9×2.''5	0.73	0.27
$J = 3-2$	345.796	33.2	JCMT	14.''5	1.0	0.2
$J = 6-5$	691.473	116.2	APEX	9.''0	1.0	0.1
$J = 7-6$	806.652	154.9	APEX	7.''7	1.0	0.3

^aMeasured in T_{A}^* , except that for the SMA, measured in the brightness temperature.

2.3. JCMT Observations

The CO (3–2) observations were retrieved from the James Clerk Maxwell Telescope³ (JCMT) archive. The data were taken on 2008 March 25 through the program M08AU19 (Maud et al. 2015). A raster map with a size of $7' \times 7'$ and a scanning spacing of $7.''3$ was obtained with the 16-pixel Heterodyne Array Receiver Program (HARP) and the Auto Correlation Spectral Imaging System (ACSIS), and the latter was configured to have a bandwidth of 1 GHz divided into 2048 channels. The JCMT beam at the frequency of CO (3–2) is about $14.''5$. The data were processed with the ORAC-DR pipeline software following the REDUCE_SCIENCE_GRADIENT recipe. The calibrated data in T_{A}^* were velocity smoothed into 1 km s^{-1} channels, and the corresponding RMS sensitivity is about 0.2 K. The intensity scale conversion from T_{A}^* to T_{mb} , whenever needed, would use a beam efficiency of 0.64, following <http://www.eaobservatory.org/jcmt/instrumentation/heterodyne/harp/>.

2.4. SMA Observations

We carried out Submillimeter Array (SMA)⁴ observations centered at (R.A., Decl.)_{J2000}=($18^{\text{h}}19^{\text{m}}11.^{\text{s}}0$, $-20^{\circ}48'20''$), approximately the tip of the southwestern lobe of the outflow seen in the APEX CO (6–5) map. The observations were made on 2017 April 12 under excellent weather conditions with the atmospheric opacity at 225 GHz ranging from 0.06 to 0.08. The array was in the Compact configuration with 7 antennas available during the observations. Each SMA antenna is now equipped with four receivers, namely 230 GHz, 240 GHz, 345 GHz, and 400 GHz receivers, and allows dual-receiver operations. We used 230 GHz and 240 GHz receivers, and both receivers were tuned to the same frequency coverage, $\sim 213.5\text{--}221.5$ GHz in the lower sideband and $\sim 229.5\text{--}237.5$ GHz in the upper sideband, to improve the signal-to-noise ratios for spectral line observations. The frequency setup covered CO (2–1) and ^{13}CO (2–1). The newly commissioned SWARM (SMA Wideband Astronomical ROACH2 Machine) correlator was used to provide a uniform spectral resolution of 140 kHz across 8 GHz per sideband per receiver. We smoothed the data by a factor of 4, resulting in a 560 kHz resolution, corresponding to $\sim 0.73 \text{ km s}^{-1}$ at 230 GHz. 3C279 and Callisto were observed as the bandpass and flux calibrators, respectively. The time-dependent gain variations were monitored through interleaving observations of two quasars, J1733-130 and J1924-292. We calibrated the data with the IDL MIR package⁵, and then output the calibrated visibilities to MIRIAD for imaging. The final CO (2–1) map has a synthesized beam with a full-width-half-maximum (FWHM) size of $4.''9 \times 2.''5$ and a position angle (PA) of -23° , and the ^{13}CO (2–1) map has a synthesized beam of $5.''3 \times 2.''3$ with a PA of -26° . The RMS sensitivity is about $0.14 \text{ Jy beam}^{-1}$ (or 0.27 K) at a velocity resolution of 0.73 km s^{-1} .

We summarize in Table 1 the key parameters of each observed CO line, including the frequency, equivalent temperature of the upper level energy, angular resolution, velocity resolution, and RMS sensitivity.

³ The James Clerk Maxwell Telescope has historically been operated by the Joint Astronomy Centre on behalf of the Science and Technology Facilities Council of the United Kingdom, the National Research Council of Canada and the Netherlands Organisation for Scientific Research.

⁴ The SMA is joint project between the Smithsonian Astrophysical Observatory and the Academia Sinica Institute of Astronomy and Astrophysics and is funded by the Smithsonian Institution and the Academia Sinica.

⁵ <https://github.com/qi-molecules/sma-mir>

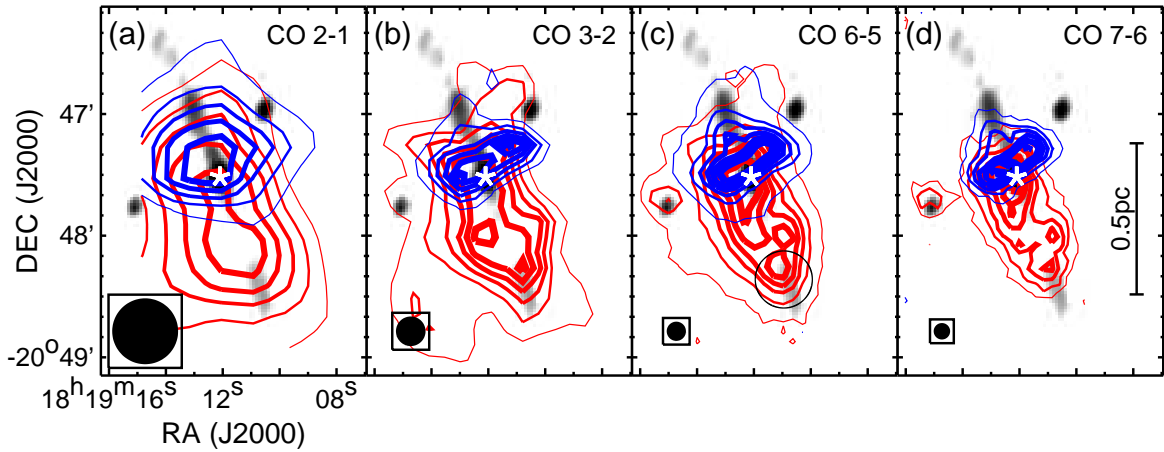


Figure 1. Velocity integrated emissions in CO lines, shown in blue and red contours for the blueshifted emission of 3 to 9 km s^{-1} and redshifted emission of 15 to 18 km s^{-1} , respectively. (a) The CSO CO (2–1) map, contouring in steps of 15% from 30% to 90% of the peaks of 36.0 and 32.9 K km s^{-1} for the blue and red lobes, respectively. (b) The JCMT CO (3–2) map, contouring in steps of 15% from 20% to 95% of the peaks of 64.0 and 42.7 K km s^{-1} for the blue and red lobes, respectively. (c) The APEX CO (6–5) map, contouring in steps of 15% from 10% to 100% of the peaks of 52.9 and 33.5 K km s^{-1} for the blue and red lobes, respectively; a circle outlines the area for computing the parameters of the collimated component of the redshifted lobe (see Section 3.4 for details). (d) The APEX CO (7–6) map, contouring in steps of 15% from 20% to 95% of the peaks of 40.0 and 23.7 K km s^{-1} for the blue and red lobes, respectively. Note that the contour thickness is proportional to the contour levels. In each panel, the grayscale shows the VLA 6 cm image of the radio jet; hereafter, an asterisk denotes the central source of the radio jet; a filled circle in the lower left corner indicates the beam size accordingly.

3. RESULTS

3.1. Single-dish CO multi-transition observations

Our single-dish observations made with the CSO, JCMT, and APEX cover the inner ~ 1 pc of the HH 80-81 radio jet. Figure 1 shows maps of velocity integrated emissions in CO (2–1), (3–2), (6–5), and (7–6), with angular resolutions of $32''$, $14''.5$, $9''$, and $7''.7$, respectively. A northeast-southwest (NE-SW) outflow with a projected length of about 0.8 pc and a P.A. of about 19° is detected in all the maps. Compared to the Very Large Array (VLA) 6 cm observations, the outflow is clearly associated with the radio jet. The outflow appears increasingly collimated in maps from low- to mid- J transitions and from low to moderately high angular resolutions. To examine whether the variation in the outflow morphology is purely due to the resolution effect, we convolve the CO (6–5) and (7–6) maps to the resolution of the CO (3–2) map, compare the maps in three lines, and find that the outflow does appear more collimated in higher excitation lines (see Appendix A). The outflow is bipolar, but very asymmetric, having a ~ 0.5 pc lobe in the SW and a much shorter, stub-like structure in the NE. This is likely due to an inhomogeneous density structure of the cloud gas around the central source. Another noticeable characteristic of the outflow is that the emission is only detected at relatively low velocities, with $-9 \lesssim v \lesssim 6 \text{ km s}^{-1}$, where v is the outflow velocity with respect to the cloud systemic velocity of 11.8 km s^{-1} (Fernández-López et al. 2011b). In the CO (3–2), (6–5), and (7–6) maps, the blueshifted emission is dominated by an elongated structure in a northwest-southeast orientation, which is mostly attributed to other outflows unrelated to the HH 80-81 radio jet (Qiu & Zhang 2009; Fernández-López et al. 2013), and will not be further discussed in this work.

Focusing on the JCMT and APEX maps of the SW lobe, the molecular outflow shows a conical, wide-angle structure within a distance of ~ 0.25 pc from the central source, and appears to re-collimate further out with the tip lying on the axis of the radio jet. To quantify the opening angle of a wide-angle structure around the radio jet, we revisit the *Spitzer* IRAC observations (Qiu et al. 2008), and measure an opening angle of $\sim 28^\circ$ ⁶. A comparison between the mid-IR cavity, the radio jet, and the CO outflow is shown in Figure 2. It seems that the molecular outflow is associated with both the highly collimated jet and the wide-angle cavity wall. Figure 3 shows the velocity channel maps of the CO (6–5) emission from 13 to 18 km s^{-1} . In channels of 14–18 km s^{-1} , the emission within a distance of

⁶ Detailed discussions on various emission mechanisms for an outflow seen in the IRAC bands, as well as a description of the IRAC observations of the HH 80–81 outflow, are presented in Qiu et al. (2008).

~ 0.25 pc from the central source traces a wide-angle component with an opening angle roughly consistent with that of the cavity wall seen in the IRAC $8\ \mu\text{m}$ image. Meanwhile, the tip of the SW lobe is seen as a clump at a distance of ~ 0.5 pc from the central source in channels of $16\text{--}18\ \text{km s}^{-1}$; the clump lies on the radio jet axis, suggesting the presence of a centrally collimated component in the molecular outflow. The channel maps of the CO (3–2) and (7–6) emissions show similar results (see Appendix B).

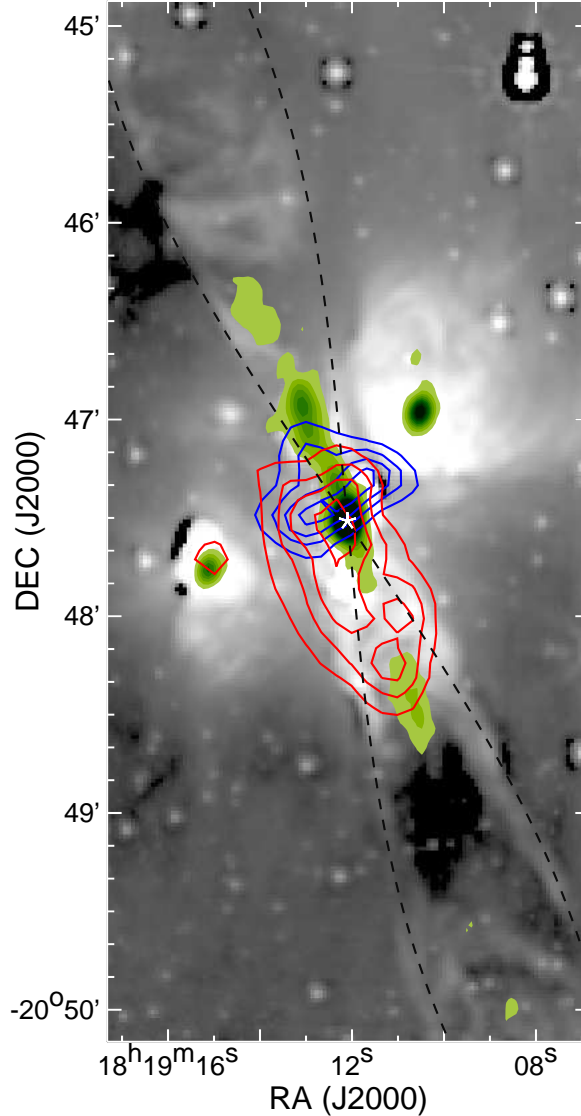


Figure 2. An overview of the *Spitzer* IRAC, APEX, and VLA observations. The grayscale background shows the IRAC $8\ \mu\text{m}$ image; we apply a high-pass filtering to the image to highlight the wide-angle wall, which is outlined with two dashed lines intersecting at the central source. Blue and red contours show the APEX CO (6–5) map, which is the same as Figure 1(c), but with contour levels starting from 30% and continuing in steps of 20% of the peak emission. Filled green contours show the VLA 6 cm continuum map starting and continuing in steps of $60\ \mu\text{Jy beam}^{-1}$.

3.2. SMA CO and ^{13}CO (2–1) observations

Previous interferometric observations toward the central source failed to unveil the outflow associated with the radio jet. This is not surprising now as we know that the outflow velocity is not very high and the low velocity CO emission around the central source is dominated by complicated structures composed of multiple outflows and ambient cloud gas. Guided by the outflow maps shown in Figure 1, we performed new SMA observations toward the tip of the SW lobe. Figure 4 shows contour maps of the velocity integrated emissions in ^{13}CO and CO (2–1), along with a

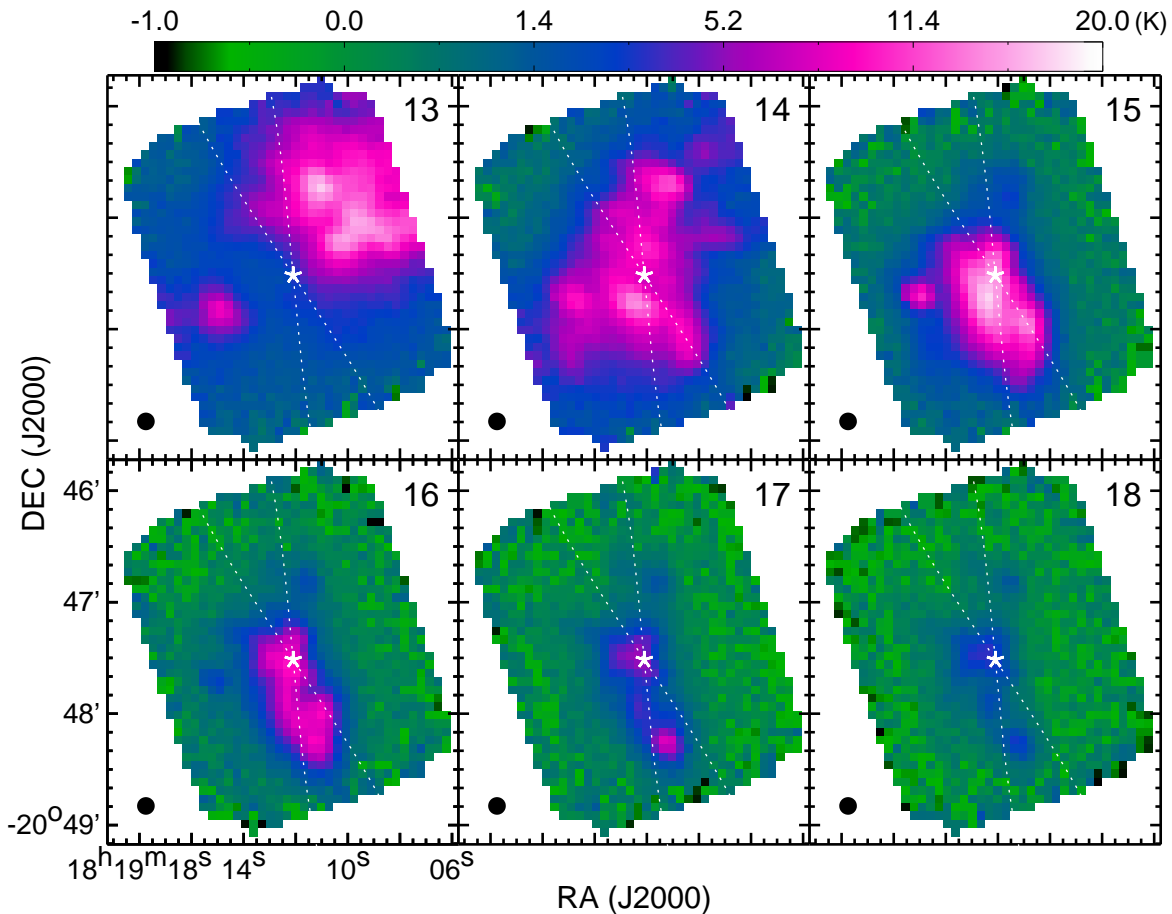


Figure 3. Velocity channel maps of the CO (6–5) emission at 13 to 18 km s^{-1} . The pseudo color scale, as indicated by a color bar on top of the figure, visualizes intensities from -1.0 to 20.0 K in T_{A}^* . Other symbols are the same as those in Figure 2.

color-composite image of the CO (6–5) outflow and the radio jet. The cavity wall seen in the *Spitzer* IRAC image is delineated by two dotted lines in Figure 4. Most recently, new sensitive and high angular resolution observations resolve the emission knots of the HH 80-81 radio jet into multiple components (Rodríguez-Kamenetzky et al. 2017). Of our particular interests are the radio knots around the SW tip of the CO (6–5) outflow, which have PAs within a range outlined by two dashed lines in Figure 4 (also see Figure 2 in Rodríguez-Kamenetzky et al. 2017). In Figure 4(a), the ^{13}CO (2–1) emission at $v = 3.58\text{--}4.31$ km s^{-1} reveals molecular structures along both the cavity wall and the radio jet. In Figures 4(b) and 4(c), the ^{13}CO (2–1) emission at $v = 5.04\text{--}6.50$ km s^{-1} and the CO (2–1) emission at $v = 2.86\text{--}6.50$ km s^{-1} trace molecular gas along and closely around the radio jet. Figure 4(d) shows the CO (2–1) emission at $v = 7.22\text{--}7.95$ km s^{-1} , which reveals molecular structures all along the radio jet at larger distances from the central source ($\gtrsim 0.5$ pc). The SMA arc second resolution observations confirm the presence of molecular outflow gas associated with both the wide-angle cavity wall and the collimated jet. And in particular, the highest velocity ($v \sim 7\text{--}8$ km s^{-1}) CO emission is clearly associated with the radio jet.

3.3. Large Velocity Gradient calculations of the outflow temperature and density

We investigate the excitation conditions of the outflow gas by performing LVG calculations of the CO line spectral energy distribution (LSED) using the RADEX code (van der Tak et al. 2007). To avoid contamination from the ambient cloud gas and other outflows from nearby high-mass protostars, we measure the CO line peaks toward the tip of the SW lobe. The H_2 temperature (T_{kin}), density (n_{H_2}), and ratio of the CO column density to the line width ($N_{\text{CO}}/\Delta V$), are derived by fitting the observed line peaks with the LVG models with a χ^2 -minimization grid search algorithm, where $\chi^2 = \sum (T_{\text{R}} - T_{\text{mb}})^2/\sigma^2$, T_{R} is the modeled line peak, T_{mb} is the measured line peak, and σ is the RMS level accordingly. Considering that the CO (2–1) map has a beam size more than two times larger than the other three lines and to mitigate the beam dilution effect, we fit the CO (3–2), (6–5), and (7–6) lines after convolving the

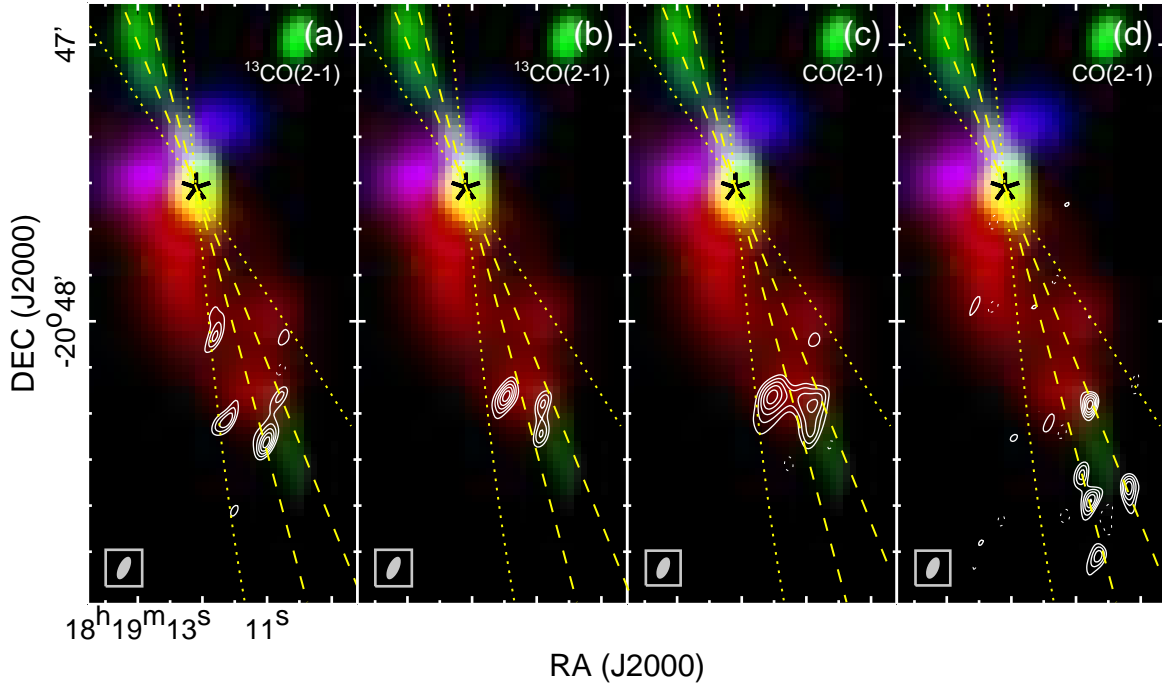


Figure 4. Contour maps of ^{13}CO (2–1) and CO (2–1) emissions observed with the SMA. (a) ^{13}CO (2–1) emission integrated from 15.38 to 16.11 km s^{-1} , contouring from 30% to 90%, by 15%, of the peak of $3.19 \text{ Jy beam}^{-1} \text{ km s}^{-1}$. (b) ^{13}CO (2–1) emission integrated from 16.84 to 18.30 km s^{-1} , contouring from 30% to 90%, by 15%, of the peak of $3.22 \text{ Jy beam}^{-1} \text{ km s}^{-1}$. (c) CO (2–1) emission integrated from 14.66 to 18.30 km s^{-1} , contouring from 30% to 90%, by 15%, of the peak of $40.62 \text{ Jy beam}^{-1} \text{ km s}^{-1}$. (d) CO (2–1) emission integrated from 19.02 to 19.75 km s^{-1} , contouring from 30% to 90%, by 15%, of the peak of $1.87 \text{ Jy beam}^{-1} \text{ km s}^{-1}$. In each panel, the background image shows the CO (6–5) outflow and the radio jet the same as those shown in Figure 2, but with the red, blue lobes of the CO (6–5) outflow, and the radio jet coded in red, blue, and green, respectively; two dotted lines outline the outflow cavity wall seen in the IRAC $8 \mu\text{m}$ image, and two dashed lines depict the range of PAs of the radio knots newly detected in Rodríguez-Kamenetzky et al. (2017); a filled ellipse in the lower left corner shows the synthesized beam at FWHM.

CO (6–5), (7–6) maps to the CO (3–2) beam. From Figure 5, the best-fit LVG model matches the observations very well, and yields $T_{\text{kin}} = 88 \text{ K}$, $n_{\text{H}_2} = 3.3 \times 10^4 \text{ cm}^{-3}$, and $N_{\text{CO}}/\Delta V = 1.3 \times 10^{16} \text{ cm}^{-2} (\text{km s}^{-1})^{-1}$. The uncertainty in the measured line peaks is dominated by the absolute flux calibration errors. If we conservatively adopt a flux calibration uncertainty of 10% for CO (3–2) and 20% for CO (6–5) and (7–6), the best-fit LVG models indicate that $T_{\text{kin}} \sim 57\text{--}112 \text{ K}$, $n_{\text{H}_2} \sim (3.3\text{--}7.8) \times 10^4 \text{ cm}^{-3}$, and $N_{\text{CO}}/\Delta V \sim (1.2\text{--}1.6) \times 10^{16} \text{ cm}^{-2} (\text{km s}^{-1})^{-1}$. Thus the outflow gas is much warmer than the ambient quiescent gas. Being about 0.5 pc from the central high-mass protostar, the gas is presumably heated by shocks which are created as the fast jet or wind impinges on the ambient cloud.

3.4. The outflow mass and energetics

We calculate the mass of the warm outflow gas with the CO (6–5) data. Provided that the blueshifted emission is dominated by other outflows unrelated to the radio jet, we calculate the mass from the redshifted emission only. By assuming optically thin emission and adopting a canonical CO-to- H_2 abundance ratio of 10^{-4} , we obtain

$$M_{\text{red}}(v) = 5.88 \times 10^{-9} \exp(116.13/T_{\text{ex}}) (T_{\text{ex}} + 0.92) d_{\text{kpc}}^2 \Delta v \int T_{\text{mb}} ds$$

where $M_{\text{red}}(v)$ is the mass in M_{\odot} of the redshifted outflow within a velocity interval of $v \rightarrow v + \Delta v$, T_{ex} is the excitation temperature, d_{kpc} is the source distance in kpc, and T_{mb} is the measured main-beam antenna temperature and is integrated over an area (measured in arc second²) encompassing the outflow. We adopt $T_{\text{ex}} = 88 \text{ K}$ based on the above LVG calculations, and obtain a mass of $1.6 M_{\odot}$ for the gas at $14\text{--}18 \text{ km s}^{-1}$. In case that the CO (6–5) emission has a moderate optical depth, τ , the mass estimate should be corrected by a factor of $\tau/(1 - e^{-\tau})$. The above LVG calculations give an optical depth of 0.68 for the CO (6–5) emission toward the tip of the SW lobe, and if we take

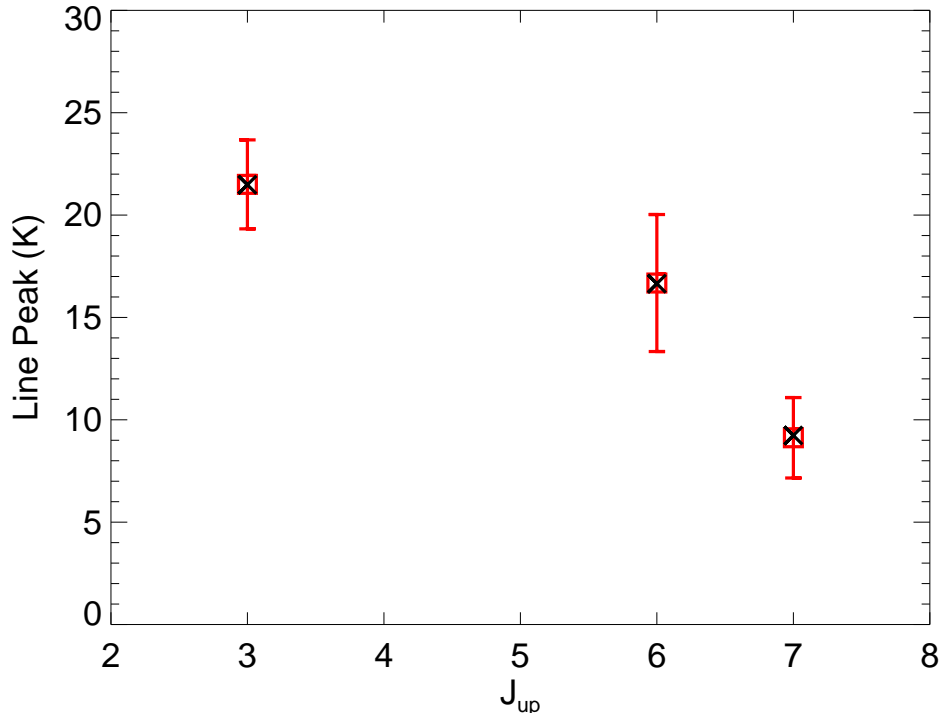


Figure 5. CO (3–2), (6–5), (7–6) line peaks ($J_{\text{up}} = 3, 6, 7$) toward the tip of the SW lobe of the outflow, with the observations shown in square symbols along with error bars taking into account both the flux calibration uncertainties and the RMS noise levels, and the best-fit LVG model shown in cross symbols.

it as an average optical depth for the entire redshifted/SW lobe, the mass of the outflow at $14\text{--}18\text{ km s}^{-1}$ amounts to $2.2 M_{\odot}$. The outflow momentum and energy are $6.8 M_{\odot} \text{ km s}^{-1}$ and 2.4×10^{44} erg, respectively. The outflow dynamical timescale, derived from the outflow length (~ 0.5 pc) divided by the maximum outflow velocity ($\sim 7\text{ km s}^{-1}$), is about 7×10^4 yr, which is consistent with that of the accretion phase of the central protostar, $(7\text{--}11) \times 10^4$ yr, and compatible with that of the dynamical age of the radio jet, $> 9 \times 10^3$ yr (Masqu e et al. 2012). Consequently, the mass loss rate is $\sim 3 \times 10^{-5} M_{\odot} \text{ yr}^{-1}$ and the outflow mechanical force is about $\sim 1 \times 10^{-4} M_{\odot} \text{ km s}^{-1} \text{ yr}^{-1}$. All the calculated parameters are listed in Table 2. The emission taken into account is confined within a polygon encompassing the outflow seen in Figure 1, and from Figure 3, the contamination from other outflows around the central source should be minor. Since the outflow is very asymmetric (Figure 1), the mass of the blueshifted/NE lobe should be small compared to that of the redshifted/SW lobe. Thus, we expect that our estimates of the outflow mass and energetics represent the lower limits of the parameters.

Given that the outflow shows a two-component structure, it is of interests to evaluate which component, collimated or wide-angle, is dominating the outflow mass and energetics. The emission shown in Figure 4(d) is coming from the central collimated component, but the SMA observations were made toward the tip of the outflow lobe, and did not cover the entire lobe (Section 2.4). Moreover, the clumpy structures seen in Figures 4 indicate that the images are affected by the spatial filtering effect of the interferometer. Thus it is difficult to obtain a reasonable estimate of the gas mass of the collimated component with the SMA data. Alternatively, by carefully examining the APEX CO (6–5) and (7–6) channel maps, we find that the two components in the redshifted lobe could be roughly separated, and in particular, the collimated component is dominated by a distant clump at $15\text{--}18\text{ km s}^{-1}$. We thus estimate the mass of the collimated component based on the CO (6–5) data. We make the calculations for the emission at $15\text{--}18\text{ km s}^{-1}$ in a circular area as outlined in Figure 1(c), adopting the same excitation temperature and optical depth as the above, and derive a mass of $0.2 M_{\odot}$. The other parameters are also computed (see Table 2). It is clear that the mass and energetics of the central collimated component are only about 10% of those of the entire lobe, indicating that the wide-angle component of the outflow is dominating the mass loss and momentum ejection to the ambient cloud.

4. DISCUSSION

Table 2. Calculated parameters of the redshifted lobe and its central collimated component

Component	Mass (M_{\odot})	Moment ($M_{\odot} \text{ km s}^{-1}$)	Energy (erg)	Length pc	Velocity (km s^{-1})	Time scale (yr)	Mass loss rate ($M_{\odot} \text{ yr}^{-1}$)	Mechanical force ($M_{\odot} \text{ km s}^{-1} \text{ yr}^{-1}$)
Redshifted lobe	2.2	6.8	2.4×10^{44}	0.5	7	7×10^4	3×10^{-5}	1×10^{-4}
Collimated	0.2	0.8	3.3×10^{43}	0.5	7	7×10^4	3×10^{-6}	1×10^{-5}

NOTE—The outflow mass and energetics may represent the lower limits of the parameters (see the discussion in Section 4.1 for more details).

4.1. Morphology, mass, and energetics of the outflow

The HH 80–81 radio jet stands out as the largest and most powerful YSO jet in our Galaxy. The molecular outflow has also been mapped by several groups using single-dish CO (1–0) and (2–1) observations (Yamashita et al. 1989; Ridge & Moore 2001; Benedettini et al. 2004; Wu et al. 2005)⁷. These observations do not have sufficient angular resolutions to resolve the outflow morphology, or to distinguish the HH 80–81 outflow from other outflows around the central source. In addition, since the outflow has relatively low velocities ($< 10 \text{ km s}^{-1}$), low- J CO maps could be easily contaminated by the ambient cloud. This is also the main reason that existing SMA observations centered at the central source failed to disentangle the outflow structure associated with the radio jet; the SMA CO (2–1) maps at low velocities suffered from side lobes and missing flux due to inadequate (u, v) coverage (Qiu & Zhang 2009; Fernández-López et al. 2013). Based on the Nobeyama 45 m telescope CO (1–0) map at a resolution of $16''$ (the highest resolution reached by previous observations of the outflow), the outflow has been thought to have a wide opening angle of 40° and does not re-collimate (Yamashita et al. 1989; Shepherd 2005; Arce et al. 2007), though the outflow axis is misaligned by about 30° from the radio jet axis. A detailed comparison between the Nobeyama CO (1–0) map (Figure 2 in Yamashita et al. 1989) and the JCMT CO (2–1) and (3–2) maps (Figure 2 in Ridge & Moore 2001, and Figure 1b in this work) indicates that the redshifted emission in the Nobeyama map is contaminated by a minor structure to the southeast seen in the JCMT maps, which along with the true redshifted lobe of the HH 80–81 outflow mimics a wide angle structure. The blueshifted emission of the Nobeyama map is presumably contaminated by other outflows around the central source (see Qiu & Zhang 2009; Fernández-López et al. 2013). Our APEX maps have a higher resolution than those of previous single-dish observations, and the relatively high excitation conditions of the CO (6–5) and (7–6) lines help to mitigate contamination from ambient quiescent clouds. Thus the APEX maps unambiguously reveal an outflow associated with the radio jet, and the outflow is overall moderately collimated, and does re-collimate at a distance of ~ 0.5 pc from the central source. The CO (6–5) velocity channel maps show that the outflow can be decomposed into two components: a wide-angle component immediately encompassing the cavity wall seen in the *Spitzer* $8 \mu\text{m}$ image within ~ 0.25 pc from the central source, and a collimated component seen as a tip lying about 0.5 pc from the central source on the radio jet axis. The latter is the first detection of the molecular counterpart of the radio jet. The “two-component” nature of the outflow is further confirmed by the SMA CO and ^{13}CO (2–1) maps, which reveal molecular knots and clumps both along the precessing radio jet and along the cavity wall.

The outflow mass derived from the CO (6–5) data is about $2.2 M_{\odot}$ for the redshifted lobe at $14\text{--}18 \text{ km s}^{-1}$, and is dominated by the wide-angle component. This is an estimate of the lower limit considering that the blueshifted lobe is not taken into account. The outflow mass ranges from 27 to $570 M_{\odot}$ in previous single-dish low- J CO observations (Yamashita et al. 1989; Ridge & Moore 2001; Benedettini et al. 2004; Wu et al. 2005; Maud et al. 2015), which is one to two orders of magnitude greater than our estimate. The discrepancy could be attributed to several reasons: previous estimates adopted a lower T_{ex} (12–40 K) and greater τ (> 1) for the CO emissions; previous low resolution CO maps were apparently contaminated by the ambient cloud and other outflows in the region; our CO (6–5) map probes a warmer and inner part of the outflow. Thus, whereas the outflow mass could be significantly

⁷ Maud et al. (2015) estimated the outflow mass and energetics based on the JCMT CO (3–2) data, but did not provide a map of the outflow.

overestimated in previous studies based on low resolution and low- J CO observations, our correction of the optical depth effect with $\tau = 0.68$ may underestimate the outflow mass by a factor of a few. Also considering the uncounted contribution from the blueshifted lobe (though it is minor based on Figures 1–3), we expect that the total mass of the CO (6–5) outflow to be on the order of a few to $10 M_{\odot}$. Consequently, the mass loss rate reaches $10^{-4} M_{\odot} \text{ yr}^{-1}$, the outflow mechanical force falls in the range of 10^{-4} to $10^{-3} M_{\odot} \text{ km s}^{-1} \text{ yr}^{-1}$, and the outflow energy amounts to 10^{45} erg. Considering empirical correlations between outflow parameters and YSO luminosities derived from low- J CO surveys of molecular outflows (Beuther et al. 2002a; Wu et al. 2004; Zhang et al. 2005; Maud et al. 2015), the time-averaged parameters (the mass loss rate and the mechanical force) of the HH 80–81 outflow appear to be a bit low, but still within the uncertainties, for a $10^4 L_{\odot}$ source. In this sense, the HH 80–81 outflow is consistent with a scaled up version of low-mass protostellar outflows (Bachiller et al. 1995; Gueth & Guilloteau 1999; Palau et al. 2006; Santiago-García et al. 2009; Hirano et al. 2010; Lee et al. 2018), showing a similar morphology but higher mass and energetics.

4.2. On the relationship between the radio jet and the molecular outflow

The HH 80–81 radio jet has been well studied over the past decades. Could the outflow be driven by the fast jet? The mass flux in the ionized jet is estimated to be $(0.6\text{--}1) \times 10^{-6} M_{\odot} \text{ yr}^{-1}$, leading to a momentum rate of $(0.6\text{--}1) \times 10^{-2} M_{\odot} \text{ km s}^{-1} \text{ yr}^{-1}$ by adopting a jet ejection velocity of $\sim 1000 \text{ km s}^{-1}$ and an ionization fraction of 0.1 (Carrasco-González et al. 2012; Rodríguez-Kamenetzky et al. 2017). Thus the thrust available from the fast jet is at least an order of magnitude greater than the mechanical force of the molecular outflow ($10^{-4}\text{--}10^{-3} M_{\odot} \text{ km s}^{-1} \text{ yr}^{-1}$), indicating that the jet is powerful enough to drive the outflow. However, the outflow shows a two-component structure in our APEX and SMA observations. The SMA map of the CO emission at higher velocities (Figure 4(d)) reveals molecular clumps lying exactly within a narrow cone being carved by the wiggling jet, providing strong evidence that the central collimated component is entrained by the jet. On the other hand, the wide-angle component has an opening angle reaching 30° , which could not be easily accounted for by the extremely collimated jet that is only gently wiggling within a few degree (Martí et al. 1993; Masqué et al. 2012). Another model that could potentially produce a wide-angle outflow shell around a collimated jet is through jet bow-shocks which are created by sideways ejections from internal shocks within the jet (Raga & Cabrit 1993; Masson & Chernin 1993). The jet bow-shock model predicts distinct velocity structures in molecular outflows: extremely high velocity features (Masson & Chernin 1993); the maximum velocities increasing with the distances from the central source in a position-velocity (PV) diagram cut along the jet axis (i.e., the “Hubble wedges”, see, e.g., Arce & Goodman 2002); a spur-like feature with the largest velocity dispersion at the largest distance to the central source in the PV diagram (Masson & Chernin 1993; Lee et al. 2001). Such velocity structures have been detected in both low-mass and high-mass outflows which are interpreted as jet bow-shock driven flows (e.g., Qiu et al. 2011, and references therein). The outflow velocities measured in the APEX and SMA maps are only a few km s^{-1} . We do not detect any high velocity ($v > 10 \text{ km s}^{-1}$) emissions in any of the CO lines. Figure 6 shows the APEX CO (6–5) PV diagram cut along the jet/outflow axis. We cannot identify any PV structure that is predicted by a jet bow-shock model. Instead the PV pattern of the SW and redshifted lobe shows a concave structure which curves outward from the point of the central source position and the cloud velocity. Such a PV structure has been observed in wide-angle outflows in both low-mass and high-mass YSOs and is consistent with the scenario that the outflow is driven by a wide-angle wind (Lee et al. 2001; Qiu et al. 2009).

Therefore, the HH 80–81 outflow cannot be understood as a purely jet driven flow. We suggest that the central collimated component and the wide-angle component each traces part of the mass flow ejected from the high-mass YSO; the mass flow consists of a fast and collimated jet (previously detected in radio continuum) and a wide-angle wind (suggested by the wide-angle component of the molecular outflow and the wide-angle cavity seen in the *Spitzer* image). It is worth noting that for low-mass outflows, the collimated component (or “molecular jets”) are typically more than 10 km s^{-1} faster than the wide-angle component, whereas in the HH 80–81 outflow, the collimated component is only $\sim 2 \text{ km s}^{-1}$ faster than the wide-angle component. Most recent ALMA observations suggest that low-mass outflows could be directly ejected from accretion disks, and thus the velocity difference between the two components manifests the difference in their launching radii on the disk (Bjerkeli et al. 2016; Lee et al. 2017; Alves et al. 2017; Tabone et al. 2017; Güdel et al. 2018). Here for the HH 80–81 outflow, the velocity of the radio jet is of order 1000 km s^{-1} (Martí et al. 1993, 1995), and as discussed above, the central collimated component of the outflow has a velocity of only $\lesssim 10 \text{ km s}^{-1}$ and should come from ambient material entrained or swept up by the jet. The velocity of the wide-angle wind is unknown, and could be estimated if extremely high angular resolution ($\lesssim 0.01''$, or $\lesssim 17 \text{ AU}$),

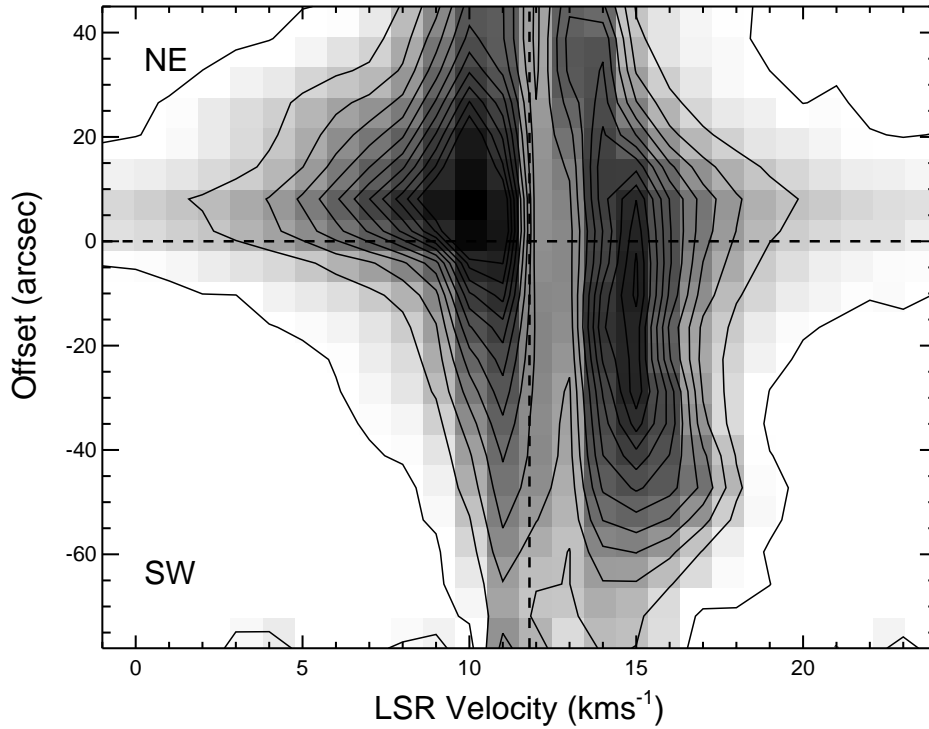


Figure 6. APEX CO (6–5) PV diagram cut along the radio jet axis. Contour levels start at 0.4 K and increase in steps of 2 K, and the grayscale image stretches from 0.4 to 19.6 K in a logarithmic scale. A horizontal dashed line indicates the position of the central source, and a vertical dashed line marks the cloud velocity of 11.8 km s^{-1} .

high sensitivity, and high fidelity observations capable of resolving the wind launching zone on the disk are available. Therefore the question about whether the wide-component of the outflow contains material directly ejected from the disk or entrained ambient gas, or both, remains open with the existing observations.

4.3. Implications to a possible evolutionary picture for outflows in high-mass YSOs

Low-mass outflows have been found to exhibit an evolutionary sequence in collimation: the outflow is highly collimated in the earliest Class 0 stages and continues to widen through late Class 0 to Class I and Class II stages (Velusamy & Langer 1998; Arce & Sargent 2006; Seale & Looney 2008; Velusamy et al. 2014; Hsieh et al. 2017). The exact mechanism responsible for the outflow broadening is not fully understood (Shang et al. 2006; Offner et al. 2011). A possible explanation invokes a relatively slow wide-angle flow around a much faster and denser axial jet ejected from the star and disk system. At the earliest stages, only the jet component can puncture the infalling envelope; as the envelope loses mass through infall and outflow, the wide-angle wind will break through and eventually become the main component; sideways splash of material from internal shocks may also contribute to broaden the outflow cavity (Arce et al. 2007; Frank et al. 2014; Bally 2016).

To account for the difference in morphology seen in some of the observed outflows in high-mass star-forming regions, Beuther & Shepherd (2005) suggested that the outflow opening angle continues to increase over time as the central high-mass YSO evolves from a protostellar stage to a hypercompact (HC) and ultracompact (UC) HII region, or alternatively, grows in mass equivalent to spectral types of mid/early-B to early-O types. It is still not well established that whether and how outflows in high-mass YSOs evolve (Qiu et al. 2008; Kuiper et al. 2016). The opening angle of the HH 80–81 outflow is 28° measured from the *Spitzer* image. The angle would be slightly larger if measured from the CO images (see Figures 2–3). This agrees with *Spitzer* observations of outflow cavities in a sample of low-mass YSOs, and could be due to entrainment of material just beyond the wall into the cavity by the wide-angle wind (Seale & Looney 2008). Compared to some well shaped massive outflows with similar scales ($\sim 1 \text{ pc}$), the HH 80–81 outflow has a moderate opening angle and a dynamical age of $7 \times 10^4 \text{ yr}$, which is larger than those of well collimated flows with dynamical ages $\lesssim 10^4 \text{ yr}$ (Beuther et al. 2002b; Qiu & Zhang 2009; Zhang et al. 2015), and smaller than those of poorly collimated flows with dynamical ages of a few 10^4 – 10^5 yr (Shepherd et al. 1998; Qiu et al. 2009).

This comparison seems to support an evolutionary sequence qualitatively similar to what is established for low-mass outflows, and further suggests that the mass ejection and accretion processes in the formation of early-B to late-O type stars could be similar to those in the formation of Sun-like stars. However, the well studied wide-angle outflows emanating from UC HII regions do not have an accompanying jet in existing observations (Shepherd et al. 1998; Qiu et al. 2009). This is different from low-mass outflows, which are known to be associated with an axial jet from Class 0 to Class II stages (Frank et al. 2014; Bally 2016). It is unclear why a jet component completely disappears in relatively later stages (e.g., the UC HII region stage) of high-mass star formation. The expansion of ionized gas and/or radiation feedback might play a role there (Keto 2002; Kuiper et al. 2016).

5. SUMMARY

We have performed CO multi-line observations of the HH 80–81 outflow using the APEX, JCMT, and CSO, as well as high resolution CO and ^{13}CO (2–1) observations using the SMA. We detect both wide-angle flows with an opening angle of about 30° , and clumps and knots following the path of the gently wiggling jet. Hence the HH 80–81 outflow is of the “two-component” nature, and the velocity structure suggests that each of the two components traces part of the mass loss process. The outflow mass and energetics estimated from the CO (6–5) data are dominated by the wide-angle component, and are significantly lower than previous estimates based on low resolution CO (1–0) and (2–1) observations, which were apparently affected by contamination from ambient cloud structures and other outflows in the region. Comparing the outflow with well shaped massive outflows available from the literature, we find that the opening angle of massive outflows continues to increase over dynamical ages of 10^3 to 10^5 yr. This is qualitatively similar to an evolutionary sequence established for low-mass outflows. However, there does exist difference in the sense that a jet component disappears in massive outflows at later stages, whereas low-mass outflows are always associated with an axial jet from Class 0 to Class II stages.

K.Q. acknowledges supports from National Natural Science Foundation of China (Grant Nos. 11473011, U1731237, 11590781, and 11629302). K.Q. is supported by National Key R&D Program of China No. 2017YFA0402600. This research used the facilities of the Canadian Astronomy Data Centre operated by the National Research Council of Canada with the support of the Canadian Space Agency.

Facility: Atacama Pathfinder EXperiment (APEX), James Clerk Maxwell Telescope (JCMT), Submillimeter Array (SMA), Caltech Submillimeter Observatory (CSO)

Software: ORAC-DR pipeline, MIR (<https://github.com/qi-molecules/sma-mir>), MIRIAD (Sault et al. 1995), RADEX code (van der Tak et al. 2007)

APPENDIX

A. COMPARISON BETWEEN THE JCMT MAP AND CONVOLVED APEX MAPS

Figure 7 shows a comparison between the velocity integrated JCMT CO (3–2) map and the APEX CO (6–5) and (7–6) maps; the APEX maps have been convolved to the angular resolution of the JCMT map.

B. CO (3–2) AND (7–6) CHANNEL MAPS

Figure 8 shows the velocity channel maps of the CO (3–2) emission, and Figure 9 shows the velocity channel maps of the CO (7–6) emission.

REFERENCES

- | | |
|--|---|
| Alves, F. O., Girart, J. M., Caselli, P. et al. 2017, A&A, 603, L3 | Bachiller, R., Guilloteau, S., Dutrey, A., Planesas, P., & Martin-Pintado, J. 1995, A&A, 299, 857 |
| Arce, H et al. 2007, PPV | Bally, J. 2016, ARA&A, 54, 491 |
| Arce, H. G. & Goodman, A. A. 2002, ApJ, 575, 928 | Bally, J., Ginsburg, A., Arce, H. et al. 2017, ApJ, 837, 60 |
| Arce, H. G. & Sargent, A. I. 2006, ApJ, 646, 1070 | Banerjee, R. & Pudritz, R. E. 2007, ApJ, 660, 479 |

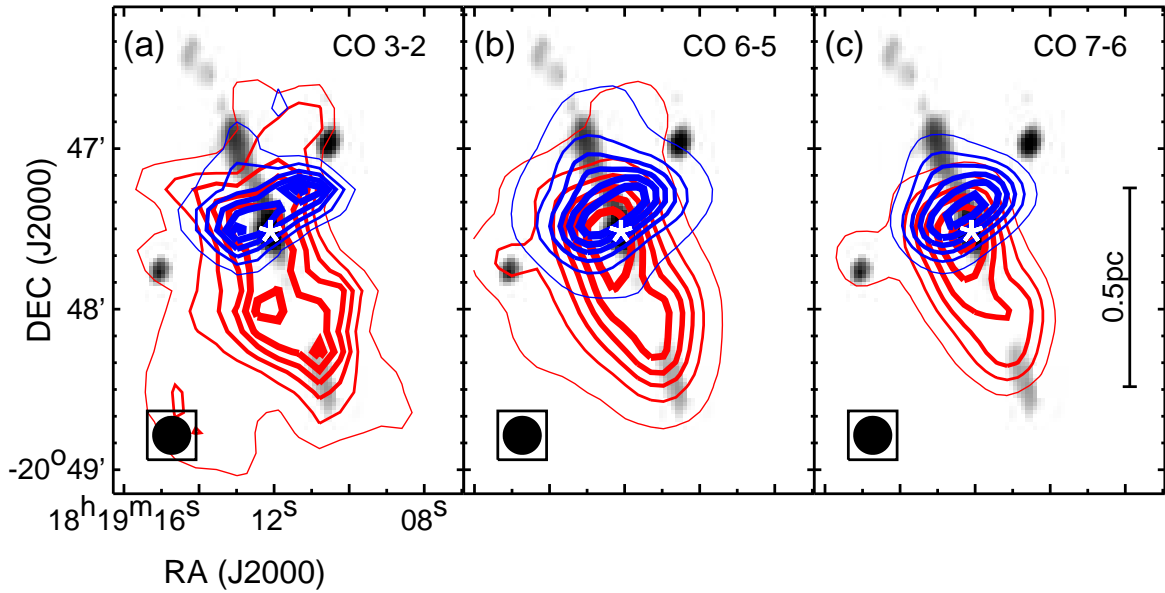


Figure 7. Velocity integrated emissions in CO (3–2), (6–5), and (7–6). (a) The same as that for Figure 1(b). (b) The same as that for Figure 1(c), except that the map has been convolved to an angular resolution of $14.''5$, and the peaks are 43.3 and 30.2 K km s^{-1} for the blue and red lobes, respectively. (c) The same as that for Figure 1(d), except that the map has been convolved to an angular resolution of $14.''5$, and the peaks are 30.5 and 20.4 K km s^{-1} for the blue and red lobes, respectively.

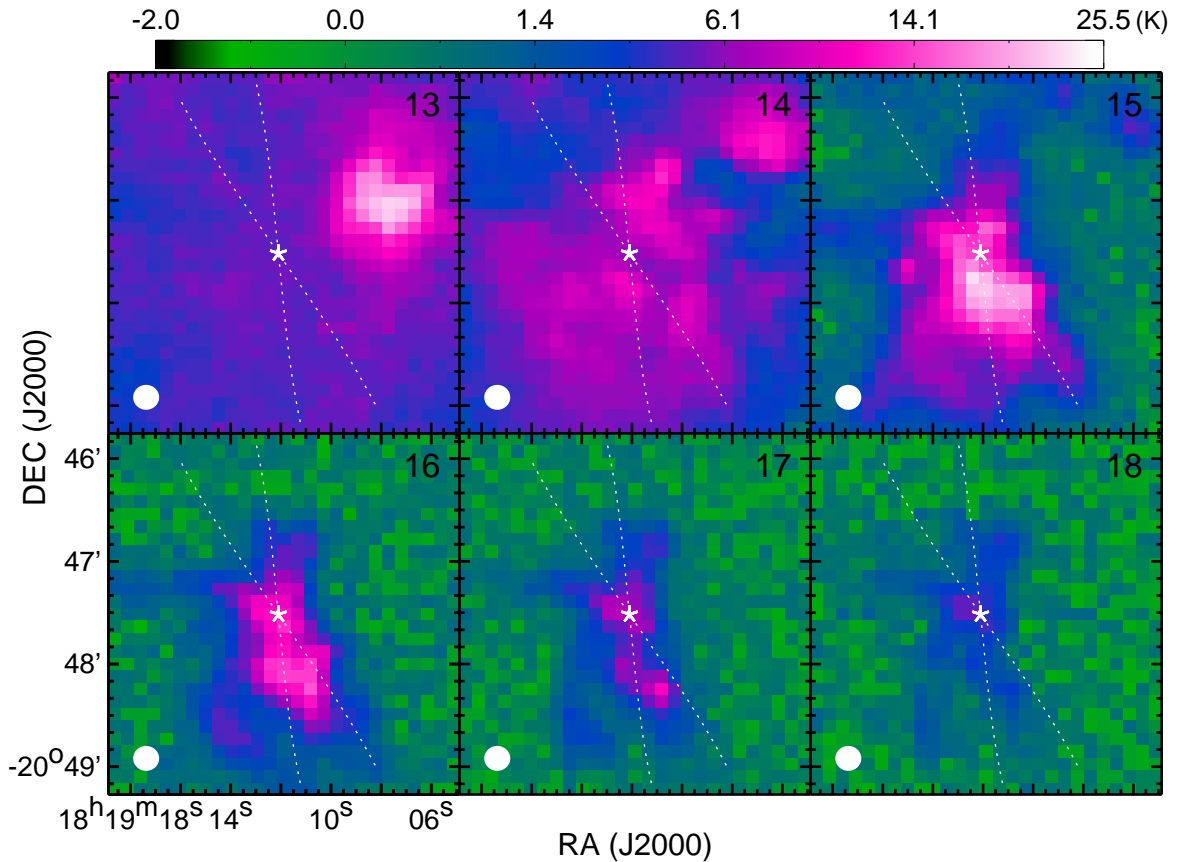


Figure 8. Velocity channel maps of the CO (3–2) emission at 13 to 18 km s^{-1} . The pseudo color scale, as indicated by a color bar on top of the figure, visualizes intensities from -2.0 to 25.5 K in T_{A}^* . Other symbols are the same as those in Figure 3.

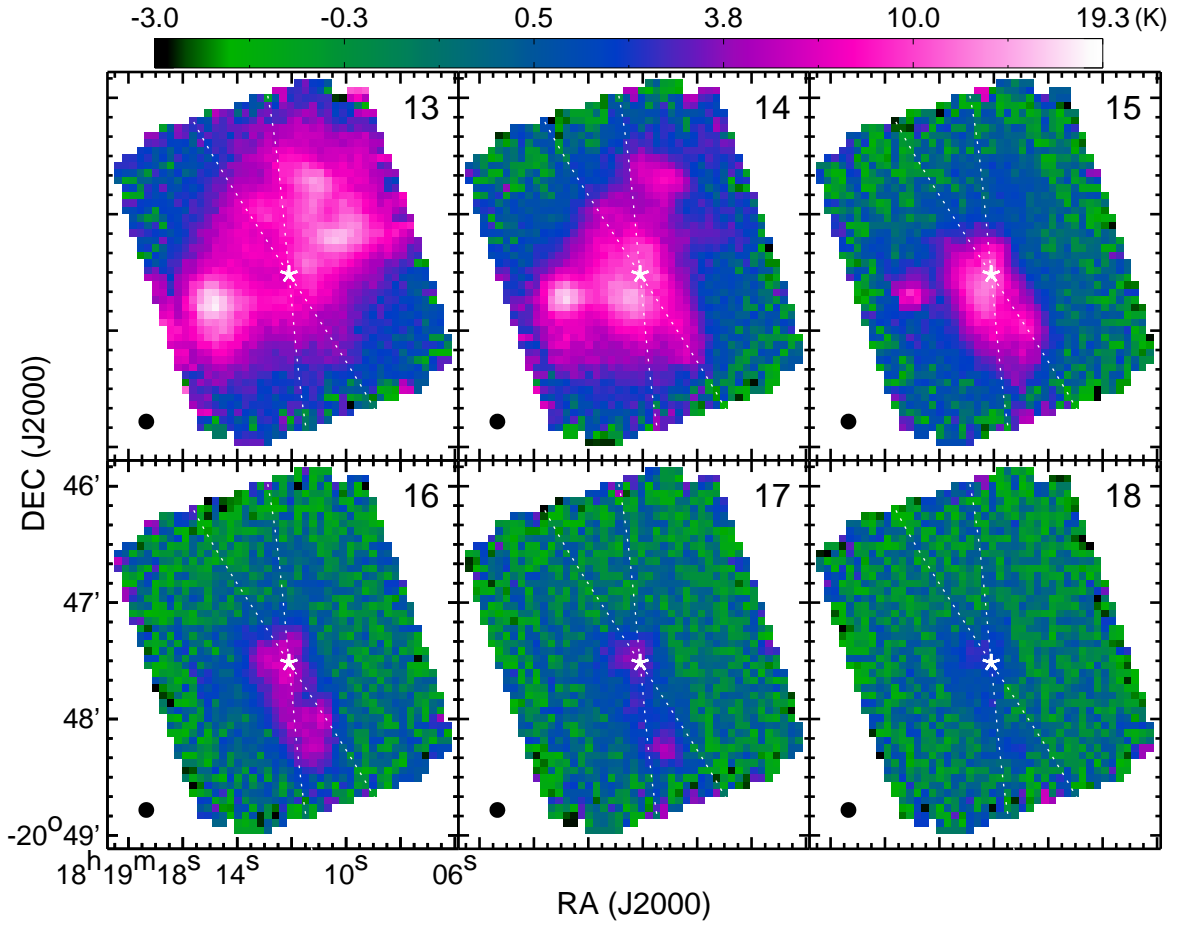


Figure 9. Velocity channel maps of the CO (7-6) emission at 13 to 18 km s^{-1} . The pseudo color scale, as indicated by a color bar on top of the figure, visualizes intensities from -3.0 to 19.3 K in T_A^* . Other symbols are the same as those in Figure 3.

- Benedettini, M., Molinari, S., Testi, L., & Noriega-Crespo, A. 2004, *MNRAS*, 347, 295
- Beuther, H., Schilke, P., Sridharan, T. K. 2002a, *A&A*, 383, 892
- Beuther, H., Schilke, P., Gueth, F. et al. 2002b, *A&A*, 387, 931
- Beuther, H. & Shepherd, D. S. 2005, in *Cores to Clusters: Star Formation with Next Generation Telescopes*, ed. M. S. N. Kumar et al. (New York: Springer), 105
- Bjerkeli, P., van der Wiel, M. H. D., Harsono, D., Ramsey, J. P., & Jørgensen, J. K. 2016, *Nature*, 540, 406
- Cabrit S., Raga A., & Gueth F. 1997, In *IAU Symposium 182: Herbig-Haro Flows and the Birth of Stars*, ed. B. Reipurth & C. Bertout (Kluwer, Dordrecht), 163
- Carrasco-González, C., Rodríguez, L. F., Anglada, G. et al. 2010, *Science*, 330, 1209
- Carrasco-González, C., Galván-Madrid, R., Anglada, G. et al. 2012, *ApJ*, 752, L29
- Carrasco-González, C., Torrelles, J. M., Cantó, J. et al. 2015, *Science*, 348, 6230
- Cesaroni, R., Felli, M., Jenness, T. et al. 1999, *A&A*, 345, 949
- Commerçon, B., Hennebelle, P., & Henning, T. 2011, *ApJL*, 742, L9
- Feng, S., Beuther, H., Zhang, Q. et al. 2016, *ApJ*, 828, 100
- Fernández-López, M., Curiel, S., Girart, J. M. et al. 2011a, *AJ*, 141, 72
- Fernández-López, M., Girart, J. M., Curiel, S. et al. 2011b, *AJ*, 142, 97
- Fernández-López, M., Girart, J. M., Curiel, S. et al. 2013, *ApJ*, 778, 72
- Frank, A. et al. 2014, *PPVI*
- Girart, J. M., Fernández-López, M., Li, Z.-Y. et al. 2018, *ApJL*, 856, L27
- Güdel, M., Eibensteiner, C., Dionatos, O. et al. 2018, *A&A*, in press, arXiv:1810.12251
- Gueth, F. & Guilloteau, S. 1999, *A&A*, 343, 571
- Heathcote, S., Reipurth, B., & Raga, A. C. 1998, *AJ*, 116, 1940
- Hennebelle, P., Commerçon, B., Joos, M. et al. 2011, *A&A*, 528, A72
- Hirano, N., Ho, P. T. P., Liu, S.-Y. 2010, *ApJ*, 717, 58
- Hirota, T., Machida, M. N., Matsushita, Y. et al. 2017, *Nature Astronomy*, 1, 0146
- Hsieh, T.-H., Lai, S.-P., Belloche, A., & Wyrowski, F. 2016, *ApJ*, 826, 68
- Hsieh, T.-H., Lai, S.-P., & Belloche, A. 2017, *AJ*, 153, 173
- Kasemann, C., Güsten, R., Heyminck, S. et al. 2006, *SPIE Conf.*, 6275, 19
- Keto, E. 2002, *ApJ*, 580, 980
- Kuiper, R., Yorke, H. W., & Turner, N. J. 2015, *ApJ*, 800, 86
- Kuiper, R., Turner, N. J., & Yorke, H. W. 2016, *ApJ*, 832, 40
- Lee, C.-F., Mundy, L. G., Reipurth, B., Ostriker, E. C., & Stone, J. M. 2000, *ApJ*, 542, 925
- Lee, C.-F., Stone, J. M., Ostriker, E. C., & Mundy, L. G. 2001, *ApJ*, 557, 429
- Lee, C.-F., Mundy, L. G., Stone, J. M., & Ostriker, E. C. 2002, *ApJ*, 576, 294
- Lee, C.-F., Ho, P. T. P., Li, Z.-Y. et al. 2017, *Nature Astronomy*, 1, 0152
- Lee, C.-F., Li, Z.-Y., Codella, C. et al. 2018, *ApJ*, 856, 14
- Li, Z.-Y. et al. 2014, *PPVI*
- Martí, J., Rodríguez, L. F., & Reipurth, B. 1993, *ApJ*, 416, 208
- Martí, J., Rodríguez, L. F., & Reipurth, B. 1995, *ApJ*, 449, 184
- Martí, J., Rodríguez, L. F., & Reipurth, B. 1998, *ApJ*, 502, 337
- Masqué, J. M., Girart, J. M., Estalella, R., Rodríguez, L. F., & Beltrán, M. T. 2012, *ApJ*, 758, L10
- Masqué, J. M., Rodríguez, L. F., Araudo, A. et al. 2015, *ApJ*, 814, 44
- Masson, C. R. & Chernin, L. M. 1993, *ApJ*, 414, 230
- Matsushita, Y., Sakurai, Y., Hosokawa, T., & Machida, N. 2018, *MNRAS*, 475, 391
- Maud, L. T., Moore, T. J. T., Lumsden, S. L. et al. 2015, *MNRAS*, 453, 645
- Offner, S. S. R., Lee, E. J., Goodman, A. A., & Arce, H. 2011, *ApJ*, 743, 91
- Peters, T., Banerjee, R., Klessen, R. S., & Mac Low M.-M. 2011, *ApJ*, 729, 72
- Palau, A., Ho, P. T. P., Zhang, Q. et al. 2006, *ApJL*, 636, L137
- Phan-Bao, N., Riaz, B., Lee, C.-F. et al. 2008, *ApJL*, 689, L141
- Plunkett, A. L., Arce, H. G., Mardones, D. et al. 2015, *Nature*, 527, 70
- Qiu, K., Zhang, Q., S. T. Megeath, et al. 2008, *ApJ*, 685, 1005
- Qiu, K. & Zhang, Q. 2009, *ApJL*, 702, 66
- Qiu, K., Zhang, Q., Wu, J., & Chen, H. 2009, *ApJ*, 696, 66
- Qiu, K., Wyrowski, F., Menten, K. M. et al. 2011, *ApJL*, 743, L25
- Raga, A. & Cabrit, S. 1993, *A&A*, 278, 267
- Reipurth, B. & Graham, J. A. 1988, *A&A*, 202, 219
- Ridge, N. A. & Moore, T. J. T. 2001, *A&A*, 378, 495
- Rodríguez, L., Moran, J. M., Ho, P. T. P., & Gottlieb, E. W. 1980, *ApJ*, 235, 845

- Rodríguez-Kamenetzky, A., Carrasco-González, C., Araudo, A. et al. 2017, *ApJ*, 851, 16
- Santiago-García, J., Tafalla, M., Johnstone, D., & Bachiller, R. 2009, *A&A*, 495, 169
- Sault, R. J., Teuben, P. J., & Wright, M. C. H. 1995, in *Astronomical Data Analysis Software and Systems IV*, ASP Conference Series, Vol. 77, ed. R.A. Shaw, H.E. Payne, and J.J.E. Hayes, 433
- Seifried, D., Pudritz, R. E., Banerjee, R., Duffin, D., & Klessen, R. S. 2012, *MNRAS*, 422, 347
- Shang, H., Allen, A., Li, Z.-Y. et al. 2006, *ApJ*, 649, 845
- Shepherd, D. S., Watson, A. M., Sargent, A. I., & Churchwell, E. 1998, *ApJ*, 507, 861
- Shepherd, D. 2005, *IAU Symposium* 227
- Seale, J. P. & Looney, L. W. 2008, *ApJ*, 675, 427
- Tabone, B., Cabrit, S., Bianchi, E., et al., 2017, *A&A*, 607, L6
- Tafalla, M., Santiago-Barcía, J., Hacar, A., & Bachiller, R. 2010, *A&A*, 522, A91
- Tafalla, M., Bachiller, R., Lefloch, B. et al. 2015, *A&A*, 573, L2
- Tan, J. C., Shuo, K., Zhang, Y. et al. 2016, *ApJL*, 821, L3
- Tobin, J. J., Stutz, A. M., Manoj, P. et al. 2016, *ApJ*, 831, 36
- van der Tak, F. F. S., Black, J. H., Schöier, F. L., Jansen, D. J., & van Dishoeck, E. F. 2007, *A&A*, 468, 627
- Velusamy, T. & Langer, W. D. 1998, *Nature*, 392, 685
- Velusamy, T., Langer, W. D., & Thompson, T. 2014, *ApJ*, 738, 6
- Vig, S., Veena, V. S., Mandal, S., Tej, A., & Ghosh, S. K. 2018, *MNRAS*, 474, 3808
- Wu, Y., Wei, Y., Zhao, M. et al. 2004, *A&A*, 426, 503
- Wu, Y., Zhang, Q., Chen, H. et al. 2005, *AJ*, 129, 330
- Yamashita, T., Suzuki, H., Kaifu, N., & Tamura, M. 1989, *ApJ*, 347, 894
- Zapata, L. A., Schmid-Burgk, J., Ho, P. T. P., Rodríguez, L. F., & Menten, K. M. 2009, *ApJL*, 704, L45
- Zhang, Q., Hunter, T. R., Brand, J. et al. 2001, *ApJL*, 552, L167
- Zhang, Q., Hunter, T. R., Brand, J. et al. 2005, *ApJ*, 625, 864
- Zhang, Q., Wang, K., Lu, X., & Jiménez-Serra, I. 2015, *ApJL*, 804, 141